Space Weather®

RESEARCH ARTICLE

10.1029/2025SW004428

Special Collection:
Space Weather Events of 2024 May 9-15

Impact of the Gannon Superstorm on the Equatorial Ionization Anomaly Dynamics During Its Recovery Phase on 11 May 2024

K. Shimna[1,2], **R. K. Archana**[1], **C. Vineeth**[1], **Gang Lu**[3], **T. K. Pant**[1], and **M. S. M. Vijayan**[4]

[1]Space Physics Laboratory, VSSC, ISRO, Trivandrum, India, [2]Krea University, Sri City, India, [3]National Centre for Atmospheric Research, High Altitude Observatory, Boulder, CO, USA, [4]CSIR Fourth Paradigm Institute, Bangalore, India

Key Points:

- Enhanced electron density along the geomagnetic equator and the absence of anomaly crests during the recovery phase of Gannon Superstorm
- An unusually intense counter-electrojet caused by disturbance dynamo inhibited fountain effects and hence formation of the anomaly crest
- Simulations revealed the presence of equatorward meridional winds which may have prevented further diffusion of plasma away from equator

Supporting Information:

Supporting Information may be found in the online version of this article.

Correspondence to:

K. Shimna,
Shimna.kan@gmail.com

Citation:

Shimna, K., Archana, R. K., Vineeth, C., Lu, G., Pant, T. K., & Vijayan, M. S. M. (2025). Impact of the Gannon Superstorm on the equatorial ionization anomaly dynamics during its recovery phase on 11 May 2024. *Space Weather*, *23*, e2025SW004428. https://doi.org/10.1029/2025SW004428

Received 10 MAR 2025
Accepted 30 OCT 2025

Author Contributions:

Conceptualization: K. Shimna
Data curation: K. Shimna
Formal analysis: K. Shimna, R. K. Archana
Methodology: K. Shimna, M. S. M. Vijayan
Software: Gang Lu, M. S. M. Vijayan
Supervision: C. Vineeth, T. K. Pant
Validation: C. Vineeth
Visualization: K. Shimna, R. K. Archana

Abstract During the recovery phase of the Gannon Superstorm on 11 May 2024, the thermosphere-ionosphere system experienced dramatic changes marked by an unusual redistribution of plasma density. The peak electron density (N_{max}) from Global-scale Observations of the Limb and Disk (GOLD), ground-based Vertical Total Electron Content (VTEC), and topside VTEC from Swarm C satellite revealed an enhanced electron density at the equator and a complete disappearance of the Equatorial Ionization Anomaly (EIA) crests. This absence of EIA crests was linked to a strong daytime Counter Electrojet (CEJ) caused by disturbance dynamo effects observed in ground magnetic data. The unusually strong CEJ suppressed the ExB vertical drift, thereby eliminating the fountain effect. Thermosphere-Ionosphere-Electrodynamics General Circulation Model (TIEGCM) simulations further indicated the presence of equatorward converging meridional winds from both hemispheres. This converging wind hindered the diffusion of plasma from the dip equatorial region, leading to the formation of a narrow band of enhanced N_{max} along the equator. Additionally, a pronounced enhancement in the $\Sigma O/N_2$ ratio along the equator was observed during the recovery phase, further contributing to this phenomenon. The present study, therefore, for the first time, demonstrates the combined effects of storm-induced changes in equatorial electrodynamics, meridional winds, and significant compositional changes during the recovery phase of a superstorm, and their influence on plasma distributions. The corroborative evidence from model simulations further strengthened these observational findings.

Plain Language Summary During the recovery phase of the Gannon geomagnetic superstorm on 11 May 2024, the peak electron density exhibited a distinctive pattern characterized by enhanced electron density at the equator, and the absence of the anomaly crests. This pattern was corroborated by electron density observations from ground and satellite measurements. Further, a significant change in the thermospheric composition is observed, that is the ratio of the column density of atomic oxygen to the column density of molecular Nitrogen, shows an enhancement at the equatorial region and extremely low ratios along mid-high latitudes. The absence of the anomaly crests is likely due to an abnormally strong westward current at equator associated with the disturbance wind from the polar region caused by joule heating. The westward electric field along the equator suppressed the crest formation. Further, the equatorward converging wind from both hemispheres inhibited the diffusion of plasma away from the equator and resulted in the formation of the equatorial narrow band of enhanced electron density. The evidence of the equatorward converging wind from both hemispheres is obtained using model simulations. The simulations also reproduced the observed enhancement of electron density at the magnetic equator, and the absence of anomaly.

1. Introduction

The recent geomagnetic superstorm of May 10–12, 2024 (Dst-index < -400 nT) stands as the strongest geomagnetic event (extreme G5) since the Halloween storms in 2003. Ground and space-based solar observatories documented a series of X-class solar flares and Earth-directed coronal mass ejections (CMEs) during this period. During geomagnetic storms, increased energy and momentum inputs at high latitudes in the upper thermosphere lead to significant heating and ion drag. These processes influence global wind patterns, causing changes in neutral composition and temperature (Li et al., 2019). Storm-time meridional winds, predominantly equatorward at high latitudes, can reach velocities of 500–800 m/s. These wind disturbances in the F-region are mainly driven by ion drag and pressure gradients (Evans et al., 2024). Apart from wind, geomagnetic storms can also alter magnetospheric convection electric fields, which can penetrate to low-equatorial latitude known as the Prompt Penetration

Writing – original draft: K. Shimna
Writing – review & editing: R. K. Archana, C. Vineeth, Gang Lu

Electric Field (PPEF) (Zhang et al., 2025 and references therein) and alter plasma distribution at low latitudes. During geomagnetic storms, Joule heating at high latitudes generates a pressure gradient, which in turn produces thermospheric neutral winds flowing equatorward and altering low-latitude electric fields through a neutral wind dynamo process, causing a Disturbance Dynamo Electric Field (DDEF) (Zhang et al., 2017 and references therein). Both PPEF and DDEF can affect the prominent features of the low-latitude ionosphere, such as EIA.

There are several studies on the impact of the superstorm of May 2024 on the ionosphere-thermospheric system. Karan et al. (2024) reported the poleward shift and merging of the EIA with aurora in the South American sector using GOLD observations. Evans et al. (2024) identified drastic changes in thermospheric composition and temperature during the recovery phase of this superstorm using GOLD observations, as well as the intense temperature gradient of 400 K between equator and pole. Themens et al. (2024) reported that strong heating and composition changes resulted in the absence of the F2 layer during the recovery phase of the May 2024 geomagnetic storm, and also reported an enhanced electron density during the main phase of the storm over the North American sector with peak height as high as 630 km. Guo et al. (2024) reported negative ionospheric storm effects in the Chinese sector during the main and recovery phases of the super-storm. From the Indian sector, using VTEC Jain et al. (2024) reported positive ionospheric storm effects in the EIA crest with ∼60% VTEC enhancement on 10th May and negative ionospheric storm effects with a depletion of VTEC by ∼68% during the recovery phase, which was attributed to the DDEF effects. Rout et al. (2024) reported that unusually strong EIA was observed at Jicamarca due to this superstorm, which lasted for 12 hr. They explained that the combined effects of a strong penetration electric field and meridional wind sustained the plasma fountains for an extended period. Zhang et al. (2024) compared the TEC responses in the Asian-Australian and American sectors during the main and recovery phases of the storm. Their results showed that during the main phase, the EIA was enhanced for approximately 9 hr in the American sector, whereas it was attenuated for about 3 hr in the Asian-Australian sector, primarily due to the effects of eastward and westward PPEF in these sectors. During the recovery phase, the Asian sector showed the effects of PPEF in ΔH. Whereas, in the American sector a dayside negative ionospheric storm is observed, which was attributed to the westward DDEF.

Previous studies have discussed the effects of geomagnetic storms on the EIA crest, where PPEF enhances the strength of EIA, and disturbance dynamo effects lead to its weakening (Pincheira et al., 2002). In a study dealing with the impact of geomagnetic storms on the post-sunset Equatorial Spread F (ESF), Tulasi Ram et al. (2008) provided observational evidence for the disappearance of the EIA and enhancement of TEC along the equatorial region during the afternoon hours (15:50 LT). Similarly, a study by Huang et al. (2010) reported signatures of positive ionospheric storms along the magnetic equator near the post-sunset period, using both theoretical and observational results. They suggested that such phenomena are seasonal and typically observed near the equinox, when summer-to-winter thermospheric winds are minimal. Earlier, Sreeja et al. (2009) reported suppression of the EIA during the recovery phase of geomagnetic storm and attributed it to westward disturbance dynamo electric field and the equatorward expansion of neutral composition changes ($\Sigma O/N_2$ depletion). However, their study was limited to daytime observations and did not address the enhancement of electron density around late evening hours along the equator. In another study, Yadav et al. (2020) reported a complete reversal of the EIA pattern during the recovery phase of a storm, attributing it to the Ionospheric nighttime enhancement over the equatorial regions associated with the plasma motions caused by the retreating anomaly.

The majority of previous studies on EIA features during the recovery phase of the geomagnetic storm have reported suppression of EIA during daytime. However, most of these studies focused either on electrodynamic processes, such as disturbance dynamo effects and storm-induced counter-electrojets (CEJs). In contrast, the present work is a comprehensive investigation using the observations from N_{max} and $\Sigma O/N_2$ ratio from GOLD satellite mission, ground-based magnetometers, ground and satellite-based TEC data, combined with TIEGCM model simulations to address the suppression of EIA and enhanced electron density over equator around twilight hours during the recovery phase of the geomagnetic storm.

2. Data and Methodology

2.1. GOLD-Based Measurements (N_{max} and $\Sigma O/N_2$)

The N_{max} and $\Sigma O/N_2$ data sets used in this study are from Level 2 data of NASA's GOLD mission (https://gold.cs.ucf.edu/search/), with data products discussed in Eastes et al. (2017, 2019) and McClintock et al. (2020). During nighttime, GOLD observes OI 135.6 nm radiance with a spectral resolution of 0.4 nm and a spatial resolution of

1° × 1° (e.g., Cai, Burns, Wang, Qian, Liu, et al., 2021; Cai, Burns, Wang, Qian, Pedatella, et al., 2021; Cai et al., 2020; Eastes et al., 2019). OI 135.6 nm radiance can be used to derive the peak electron density of the ionospheric F2 region ($N_{\max}$) (DeMajistre et al., 2004).

The intensity ratio of 135.6 nm (135–137 nm) to Lyman-Birge-Hopfield (LBH) emissions (140.5–148 nm), as observed by GOLD during disk scans, is used to derive the column density ratio $\Sigma O/N_2$, which is included in the GOLD Level 2 data product. $\Sigma O/N_2$ represents the ratio of column density of atomic oxygen (O) to column density of molecular nitrogen (N2), referenced to an N_2 column depth of 10–17 cm^{-2}, and has a temporal resolution of 2 hr. The concept of $\Sigma O/N_2$ was introduced and discussed by Strickland et al. (1995) and Evans et al. (1995), with a detailed description of the GOLD $\Sigma O/N_2$ algorithm provided by Correira et al. (2021).

2.2. Ground-Based VTEC and Top-Side VTEC Data

To corroborate the GOLD observations, TEC was computed using the phase and code measurements observed at various international GNSS Network (IGS) stations (Table S1 in Supporting Information S1). Dual frequency GPS measurements of the IGS stations obtained from the data repository (https://www.unavco.org/data/gps-gnss/data-access-methods/gnss-data-access-notebooks/gnss-permanent-station-data-access-notebook-embed.html) were converted to Slant TEC (sTEC) by carrying out phase leveling along the phase connected arc for each satellite-receiver link using IONODTECT software (Catherine et al., 2015; Vijayan et al., 2013). The detailed description of computing sTEC and mapping the sTEC into vertical TEC (vTEC) is given in Shimna and Vijayan (2020).

The Swarm mission comprises three satellites, Swarm Alpha (A), Swarm Beta (B), and Swarm Charlie (C), designed to study Earth's magnetic field, ionosphere, and space weather. These satellites orbit at altitudes of 450 km (Swarm A and C) and 530 km (Swarm B), with inclinations of 87.4° and 87.5°, respectively. Equipped with GPS receivers, the satellites measure Total Electron Content (TEC) at a frequency of 1 Hz. TEC data, which represent the number of electrons along the signal path between the satellite and the GPS receiver, can be accessed via ESA's data portal https://earth.esa.int/eogateway/catalog/swarm-ionosphere-magnetosphere.

2.3. Ground-Based Geomagnetic Data

The one-minute sampled geomagnetic horizontal component data from TTB and KOU stations, detailed in Table S2 in Supporting Information S1, were obtained from the INTERMAGNET website (https://intermagnet.org/). The diurnal variations in the geomagnetic horizontal component (ΔH) were calculated by subtracting the local midnight mean values from the data. The difference between ΔH at TTB (a geomagnetic equatorial station) and ΔH at KOU (a low-latitude station) was used to infer the strength of the Equatorial Electrojet (EEJ) at TTB.

To examine the presence of the PPEF, the east–west component of the interplanetary electric field (Ey) was obtained from the OMNI web (https://omniweb.gsfc.nasa.gov/). In addition, the real-time prediction of the PPEF as a function of longitude, with a temporal resolution of 5 min, based on Manoj et al. (2008), was utilized. This model uses solar wind parameters at the L1 point and a transfer function derived from 8 years of data from the JULIA radar, the interplanetary electric field (IEF), and the magnetometer onboard the CHAMP satellite (Manoj & Maus, 2012). The penetration electric field obtained from this Prompt Penetration Equatorial Electric Field Model (PPEEFM) over the longitude of 50°W was used in this study for comparison with ground-based magnetic observations. The model is accessible at https://geomag.colorado.edu/online-calculators/real-time-model-ionospheric-electric-fields. The magnetic signatures associated with disturbance dynamo electric fields (DDEF) were computed following the methods described in Bulusu et al. (2018, 2020). The Dst and Kp indices were also obtained from the OMNI website (https://imag-data.bgs.ac.uk/GIN_V1/GINForms2).

2.4. Thermosphere-Ionosphere-Electrodynamics General Circulation Model (TIEGCM)

The neutral meridional wind, TEC and $\Sigma O/N_2$ in the study region during the observed phenomena were examined using a first-principles, 3D, self-consistent nonlinear representation of the thermosphere-ionosphere system via the TIEGCM (Qian et al., 2014; Richmond et al., 1992; Roble et al., 1988). The AMIE (Richmond & Kamide, 1988) outputs of plasma convection and auroral precipitation patterns are used to drive the TIEGCM for the 11 May 2024 event. The TIEGCM used in the present study has a 1.25° horizontal resolution, 1/4 scale height vertical resolution, and spans ~97–700 km in altitude.

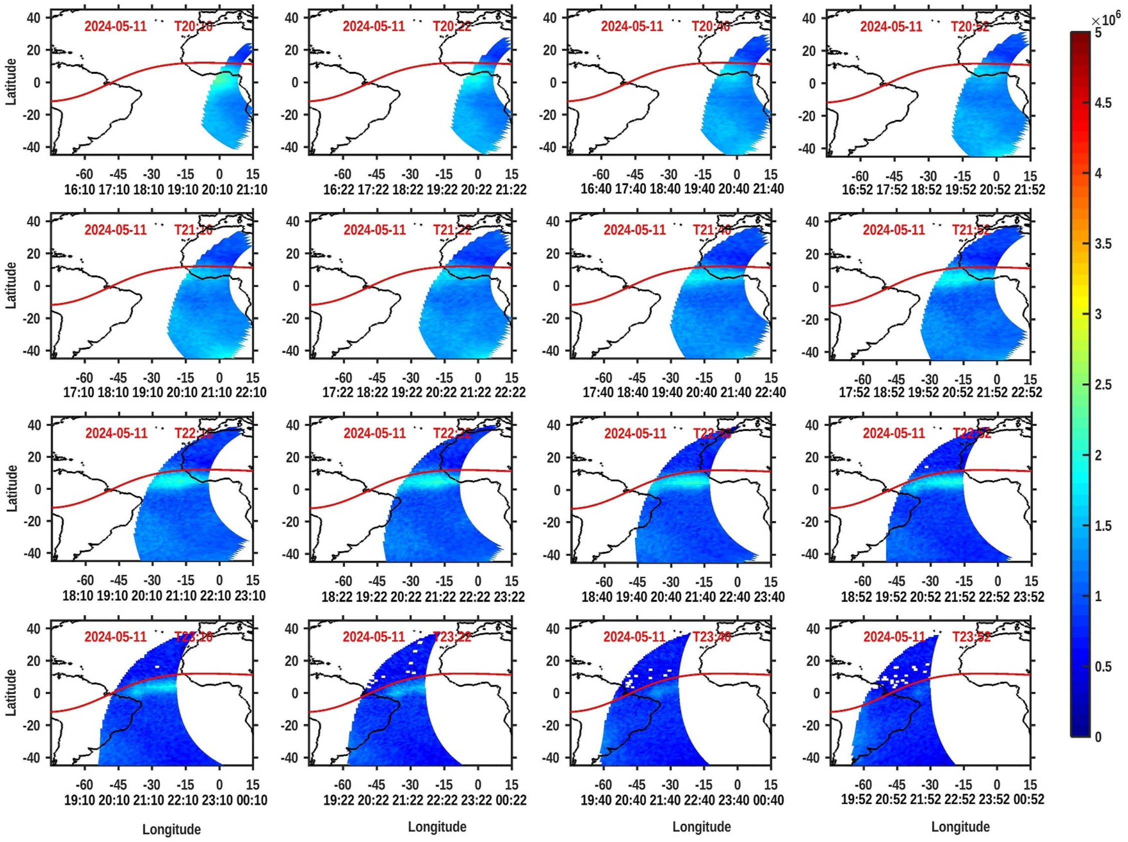

Figure 1. Spatio-temporal variation of peak electron density (el/cc) scan from GOLD observations on 11 May 2024 from 20:10 UT to 23:52 UT. Color code represents the variation of N_{max}. The red line represents the location of the geomagnetic equator and the white pixels indicate no valid data points are there on those locations. Local time is represented corresponding to each longitude at the bottom of each panel.

3. Observations

3.1. Unusual Spatial Distribution of Ionosphere Parameters Based on GOLD Observations

To study the impact of the geomagnetic storm of 10 and 11 May 2024, on the Equatorial Ionization Anomaly (EIA), the spatio-temporal variation of peak electron density (N_{max}) obtained from GOLD observations on 11 and 12 May 2024, was analyzed and is shown in Figures 1 and 2. The GOLD's N_{max} observation was made during twilight hours, depicted in Figure 1, spanning from 20:10 UT to 23:52 UT (twilight hours) on 11 May 2024, during the recovery phase of the geomagnetic storm. Similarly, on 12 May 2024, the GOLD scan covered the same time range. Figure 1 shows a complete absence of the EIA crest from 20:10 UT to 23:52 UT on May 11, whereas well-developed EIA crests are evident on May 12 (Figure 2).

The spatial distribution of peak electron density at 20:10 UT on May 11 reveals a spatially diffused electron density, with an enhancement near the magnetic equator, which is unlike the traditional EIA with two off-equator electron density crests. However, an enhanced peak electron density of 2.8×10^6 el/cc is observed just south of the geomagnetic equator. As the scan progresses, the electron density shifts toward the equator, forming a narrow, intense peak. The formation of this narrow band of increased electron density near the magnetic equator becomes prominent by 21:40 UT. By 23:40 UT, the electron density has fully dissipated, resulting in a uniform distribution of peak electron density of 0.5×10^6 el/cc across the scan. The percentage deviation of uncertainty for the peak electron density measured by the GOLD mission is presented in Figure S10 of Supporting Information S1, along with the formula used for its computation. To further confirm the spatial variation of the observed peak electron density, the latitudinal profiles for the quiet and disturbed days at different times are shown in Figure S12 of Supporting Information S1.

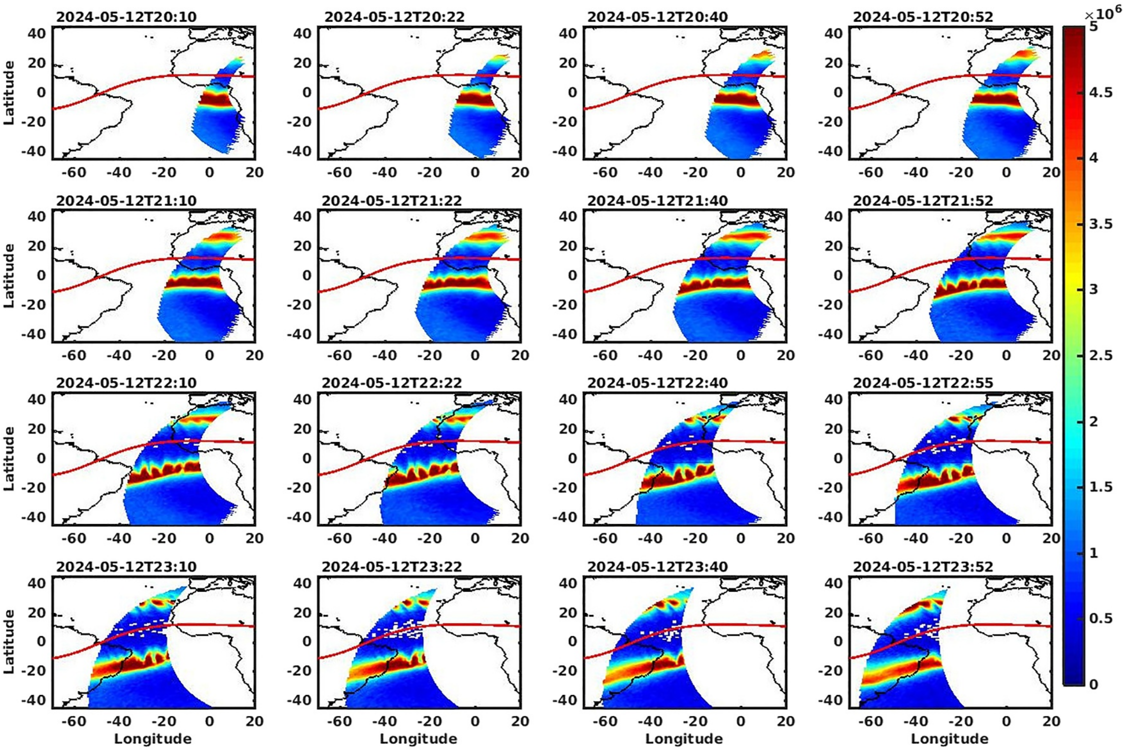

Figure 2. Spatio-temporal variation of peak electron density (el/cc) scan from GOLD observations on 12 May 2024 from 20:10 UT to 23:52 UT. Color code represents the variation of $N_{\max}$. The red line represents the location of the geomagnetic equator, and the white pixels indicate that no valid data points are there at those locations.

3.2. Absence of the EIA Crests and Enhancement of Electron Density Along the Equator—Observations From Ground and Satellite

The observations from GOLD were verified by topside TEC measurements from ground and Swarm C satellite. Figure S4 in Supporting Information S1 depicts the spatial distribution of vertical TEC variations for the stations listed in Table S1 in Supporting Information S1 on 11 and 12 May 2024. On May 11 (Figure S4 in Supporting Information S1 left panel), the vertical TEC shows the absence of the EIA crests, with enhanced electron density concentrated around the geomagnetic equator. The maximum TEC at the equator reaches approximately 50 TECU. In contrast, on May 12, well-developed EIA crests can be clearly seen, with a peak intensity of 100 TECU (Figure S4 in Supporting Information S1 right panel) along the crests.

To investigate the absence of the EIA crest in more detail, the mean vertical TEC variations at the nominal crest and trough locations were analyzed for individual stations (Figure 3). The selected stations are SAVO (southern crest), ABMF (northern crest), and BELE (equator). Between 0:00 and 4:00 UT (~23:50 LT on May 10), SAVO and ABMF record elevated TEC values of 48 and 30 TECU, respectively, which could be due to the impact of main phase of the geomagnetic storm, Sym-H reached its negative peak of −518 nT at ~02:14 UT, on 11th May (Tulasi Ram et al., 2024). After 5:00 UT, TEC at the crest regions declines significantly, remaining below 20 TECU throughout the day. In contrast, the equatorial station BELE exhibits an increasing trend on the same day, with TEC peaking at 50 TECU around 15:00 UT. To analyze storm-time changes, the difference between a disturbed day and a quiet day is considered, along with the percentage deviation in TEC, calculated using the following formula:

$$\%\ \text{Deviation TEC}\ (t) = [\text{TEC(disturbed)} - \text{TEC(quiet)}]/\text{TEC(quiet)}\, X100$$

On 11 May, after 10 UT, a pronounced negative deviation in TEC was observed at ABMF and SAVO, indicating a substantial reduction over the anomaly crest region compared with quiet-day conditions. In contrast, the equatorial station BELE showed an enhancement in TEC, with a deviation of about −40%, while the anomaly crest

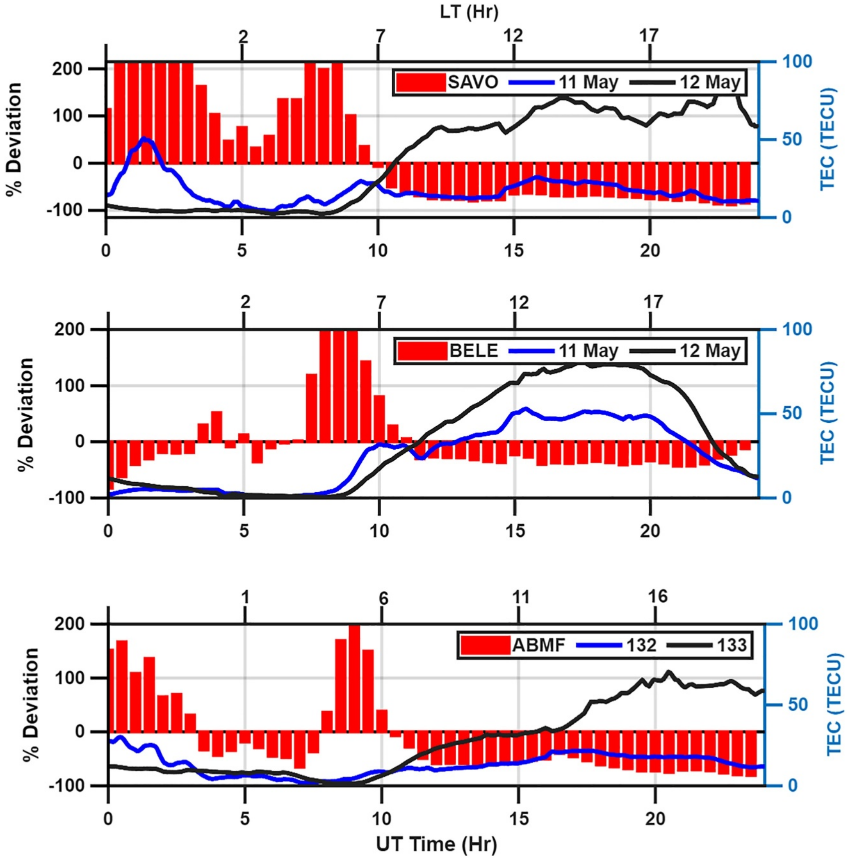

Figure 3. Mean vertical TEC variation on 11 and 12 May 2024 at selected stations SAVO, ABMF, and BELE (right axes) and Percentage deviation of TEC (left axes). Local time at each station is mentioned at the top of the panel.

region experienced a much stronger decrease of nearly −80%. This contrast highlights the relative enhancement of TEC at the equatorial region compared to the crest locations.

The topside vertical TEC (VTEC) measured by the Swarm C satellite during its passes over the South American sector (±60° latitude, 60°W–10°E longitude). The VTEC from the passes averaged over each 2° latitude on 11 and 12 May 2024, is presented in Figure 4. The Swarm C satellite recorded two passes after 20:00 UT on both days, coinciding with the availability of GOLD $N_{\max}$ measurements, the equatorial passing of the satellite was around ~19:00LT. The percentage of deviation of VTEC on 11 from quiet day 12 May is shown as a bar plot.

On May 11, the topside TEC was notably low, with the maximum VTEC observed near the equator an amplitude of ~20 TECU and no evidence of an EIA crest was detected on this day. In contrast, on May 12, revealed two distinct TEC peaks, indicating the formation of EIA crests. The peak VTEC of more than 55 TECU was observed along 20°N, and another peak of 45 TECU near 0° latitude. The deviation bars show a significant difference in TEC distribution between the days, along the northern crest a difference of 75% of TEC noted, while in the southern crest difference is around 65%. Significant deviation in TEC is also observed along the equatorial region with a difference of ~60%, confirming that the significant reduction in TEC on 11 May, occurred through equatorial-low and mid latitude regions of the sector compared to 12 May.

3.3. Changes in the Thermospheric Composition

The variation in the thermospheric column density ratio of atomic oxygen (O) to molecular nitrogen (N_2) ($\Sigma O/N_2$) derived from GOLD observations on 11 May 2024, as shown in Figure 5. The scans were conducted from 08:10 UT to 18:10 UT at 2-hr intervals.

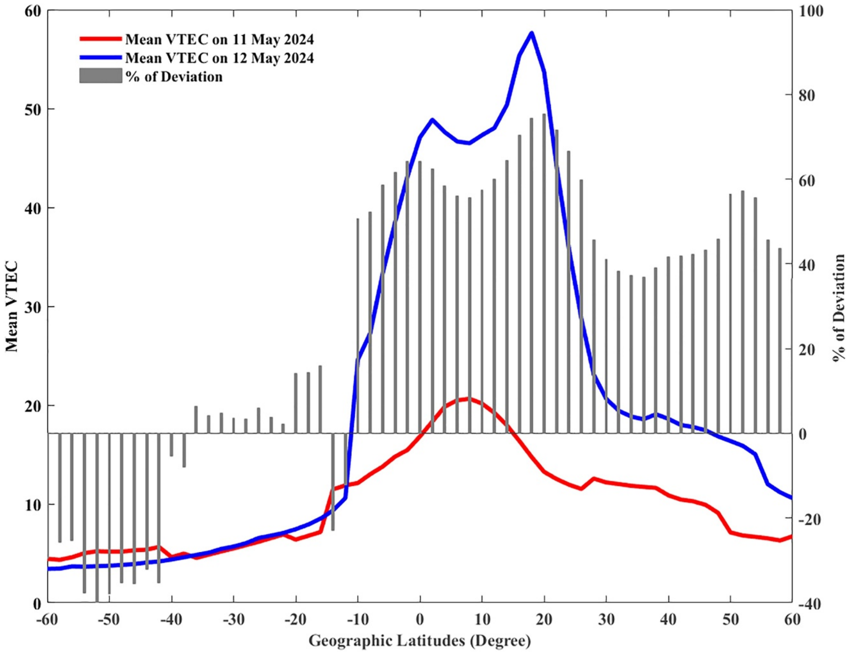

Figure 4. The averaged latitudinal variation of VTEC along the Swarm-C passages on May 11 and 12 along the American sector, the percentage of deviation of VTEC on 11 May from 12 May also presented.

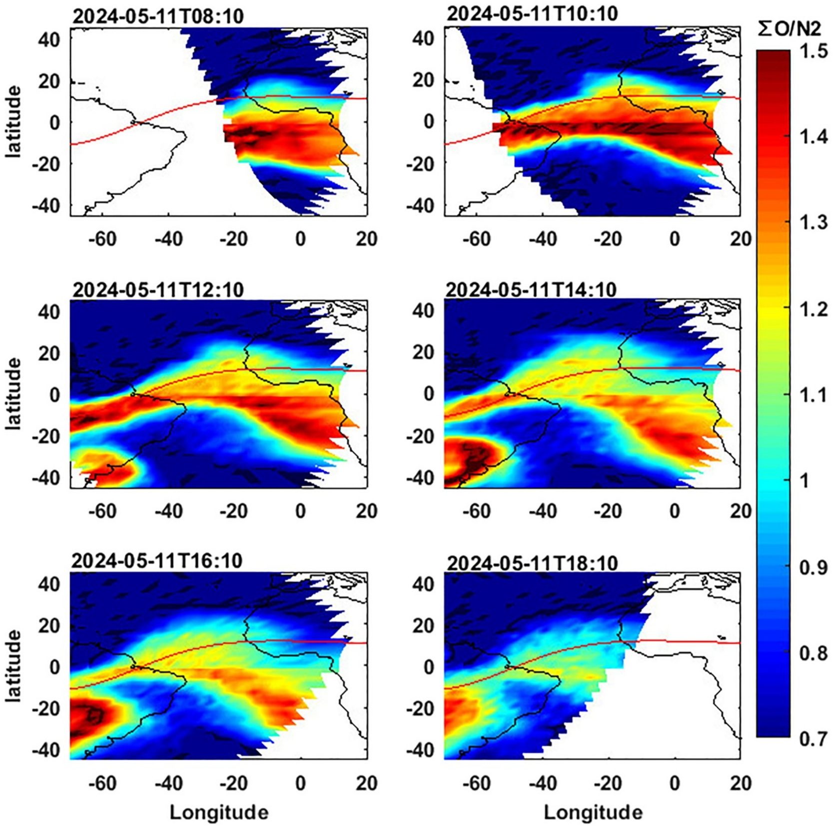

Figure 5. The thermospheric column density ratio of atomic oxygen (O) to molecular nitrogen (N_2) ($\Sigma O/N_2$) obtained from GOLD observations on 11 May 2024 from 08:10 UT to 18:10 UT. The red line represents the location of the geomagnetic equator.

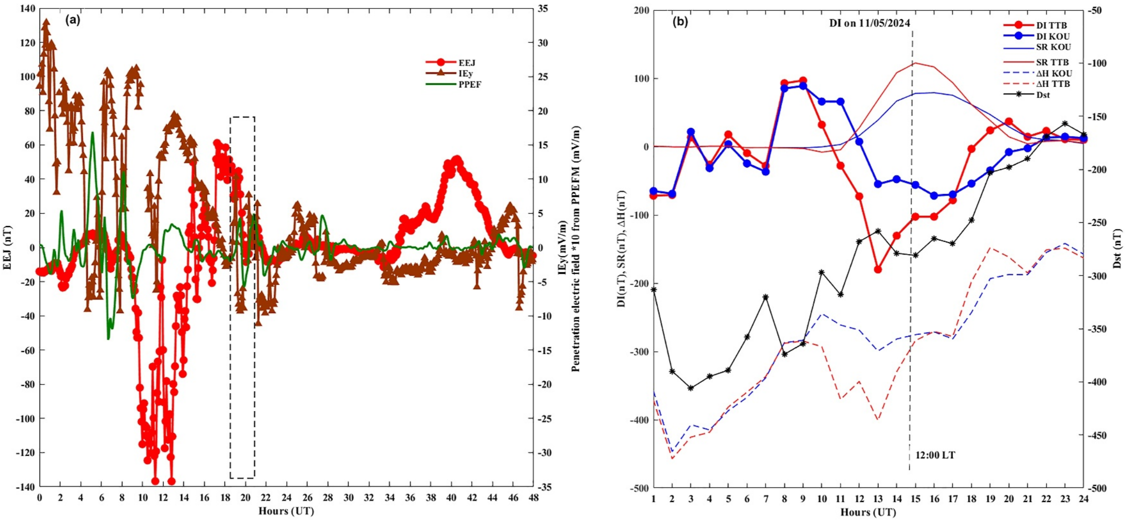

Figure 6. (a) The 5-min sampled EEJ, Interplanetary electric field east-west (Ey) and Penetration electric field (PEF) from the model at TTB for 11–12 May 2024. The identified PPEF event is highlighted by dash rectangle (b) Magnetic signature associated with DI, SR, and Dst variations.

The scan at 08:10 UT revealed a band of enhanced $\Sigma O/N_2$ (>1.5) located south of the geomagnetic equator, with a latitudinal spread of approximately 25°. By around 10:10 UT, the band had shifted closer to the geomagnetic equator, with a slight narrowing in width to about 18° (Figure 5). By 18:10 UT, the band of enhanced $\Sigma O/N_2$ had merged along the geomagnetic equator, exhibiting a reduced intensity. The percentage deviation of the thermospheric composition obtained from the GOLD mission is presented in Figure S11 of Supporting Information S1.

3.4. The Presence of an Intense Equatorial Counter-Electrojet During the Recovery Phase

As the equatorial electric field has a direct impact on the EIA characteristics, the response of the equatorial ionosphere to the recovery phase of the storm has been examined using ground magnetic data. The major source of disturbances at the equatorial region during the recovery phase of the storm is by disturbance electric field from high latitudes, which again can be due to PPEF or DDEF or by both (also it is impossible to separate the signatures of PPEF and DDEF Manoj et al. (2008)).

To identify short-term fluctuations in the EEJ caused by the PPEF, five-minute sampled EEJ strength at TTB was compared with the Ey component of solar wind and the PEF from the PPEFM model, are presented in Figure 6a. The matching fluctuations around 20:00 UT on 11 May in EEJ, Ey, and PEF indicate a prompt penetration event. The event began around 19:20 UT and the oscillations ended around 20:49 UT, during the event Ey amplitudes changed from 10 to −8 mV/m, EEJ decreased from 38 to −8 nT, and the modeled PEF varied from 0.44 to −0.57 mV/m. Although Ey and modeled PEF show significant fluctuations between 06:00–09:00 UT, these are not reflected in the ground magnetic data. At that time, the corresponding local time at TTB was 03:00–09:00 LT, when ionospheric conductivity is low. The EEJ strength was mostly negative on 11 May, indicating the presence of CEJ. Around 10:00–12:00 UT, the CEJ amplitude reached a maximum (∼−140 nT). At this time (∼09:00 LT), ionization had already started.

During the CEJ event, several intense short-term fluctuations were observed in the EEJ that did not correspond well with either PEF or Ey, confirming that the observed CEJ is not caused by PPEF. By 15:00 UT (corresponding to local noon, ∼12:00 LT), EEJ strength reached ∼60 nT, indicating the disappearance of CEJ and appearance of EEJ. On May 12, the EEJ signature returned to normal, with a noon-time peak of approximately 50 nT observed and no significant matching fluctuations among EEJ, Ey, and PEF were observed.

To identify the presence of DDEF, further analysis has been carried out on ground magnetic data. The magnetic signature of the disturbance electric field effects is extracted using conventional methods employed by Le Huy and Amory-Mazaudier (2005) and Bulusu et al. (2018, 2020). The combined effects of disturbance dynamo and prompt penetration can be computed using the equation $DI = \Delta H - SR - Dst \times \cos(L)$, where ΔH is the diurnal variation on the given day, SR is the diurnal variation on the closest quiet day represents solar quiet time variations (Sq), and L is the magnetic latitude. Using the Dst index and magnetic latitude, the correction for the ring current contribution has been applied at each site. The ΔH on 14 May represents SR the quiet-time Sq current. To extract the magnetic signatures associated with disturbance electric fields, the background quiet-time Sq components and ring current effects were eliminated. The remaining magnetic variations are attributed to perturbations from high-latitude disturbance electric fields.

In the present study, the DI signature at the equatorial site TTB and the low-latitude site KOU is computed for May 11 using the same equation, with ΔH from May 14 is the best next quiet day and considered as a reference (SR) Sq variation. The Kp and Dst variations on 14th May are provided in Supporting Information S1 (Figure S8). Figure 6b presents the computed DI at TTB and KOU, ΔH at both sites on May 11, as well as the Dst values for May 11. The DI signatures at both sites show a westward current after 11:00 UT, with enhanced amplitude at TTB compared to KOU. The westward DI shows a sharp variation around 13:00 UT at TTB, where the amplitudes of DI go below the lower limit (mean-2*std) presented in Supporting Information S1 (Figure S8). At the corresponding time, Dst does not exhibit similar changes, confirming that the enhanced westward current is not due to the ring current. The westward current observed between 8:00 and 17:00 UT at TTB is significantly stronger than at KOU, with a difference of more than 100 nT between the sites. During this period no PPEF was noted from Figure 6a, confirming the DI signatures might be due to disturbance dynamo alone.

All geomagnetic data used in this study are quasi-definitive data from INTERMAGNET observatories. According to INTERMAGNET standards, the uncertainty is within ±5 nT (Peltier & Chulliat, 2010); therefore, the possible uncertainty associated with ΔH and SR is expected to be of the same order. Katus and Liemohn (2013) reported that uncertainties in the Dst/Sym-H indices can reach ∼10 nT during quiet times and may increase to nearly 20% during storm peaks. Earlier, Clauer et al. (1980) estimated that the random error in low- to mid-latitude perturbations under quiet conditions is typically about ±6 nT, primarily due to uncertainties in the Sq current system. In the present study, the computation of DI from ΔH required the Dst index; hence, the uncertainty associated with DI is estimated to be ≤20%.

3.5. Corroborative Evidence From TIEGCM Simulation

Figure 7a shows the meridional wind pattern obtained from the TIEGCM simulation at ∼320 km altitude corresponding to the time of the GOLD observation. Positive wind values indicate northward wind, whereas negative values represent southward wind. At 20:00 UT, a strong northward wind is observed blowing toward the equator from approximately 60°S. Simultaneously, in the Northern Hemisphere, a strong southward wind is also present. As time progresses, the oppositely directed winds from the two hemispheres approach toward each other near the equator; after about 23:00 UT, the meridional winds weaken.

Figure 7b presents the Total Electron Content (TEC) obtained from the TIEGCM simulation ∼at 320 km altitude. The simulation produces a pattern similar to GOLD's $N_{\max}$ observation, showing an enhancement in TEC at the equator. As time progresses, the intensity of the simulated TEC decreases relative to the initial observation, which is also in accordance with the GOLD observation. Furthermore, the simulation reproduced the recovered characteristics of the I–T system on 12 May, indicating a well-developed EIA, as shown in Figure S13 of Supporting Information S1.

Similarly, Figure 7c presents the TIEGCM-simulated thermospheric composition closely corresponding to the GOLD $\Sigma O/N_2$ observations (∼160 km). The simulation reveals a distinct enhancement in $\Sigma O/N_2$ across the low-latitude region, extending approximately from 30°S to 30°N. In comparison, the GOLD observations show the enhancement more confined to the equatorial region, while the model depicts it over a broader area. Nonetheless, the equatorial enhancement in the simulation is consistent with the latitudinal pattern observed by GOLD, suggesting that the model reasonably reproduces the large-scale compositional variations in the equatorial and low-latitude thermosphere. It should be noted that the TIEGCM model systematically overestimates the GOLD-derived $\Sigma O/N_2$ values in the northern hemisphere. This discrepancy may arise from several factors. The empirical high-latitude forcing and neutral composition inputs used in the model may not fully capture the hemispheric asymmetries in thermospheric dynamics and composition, particularly during disturbed conditions. In contrast, the GOLD observations represent instantaneous and localized measurements that inherently include both short-term variability and longitudinal structure, which may not be fully resolved by the model's global and

a) TIEGCM simulated meridiional wind at ~320km

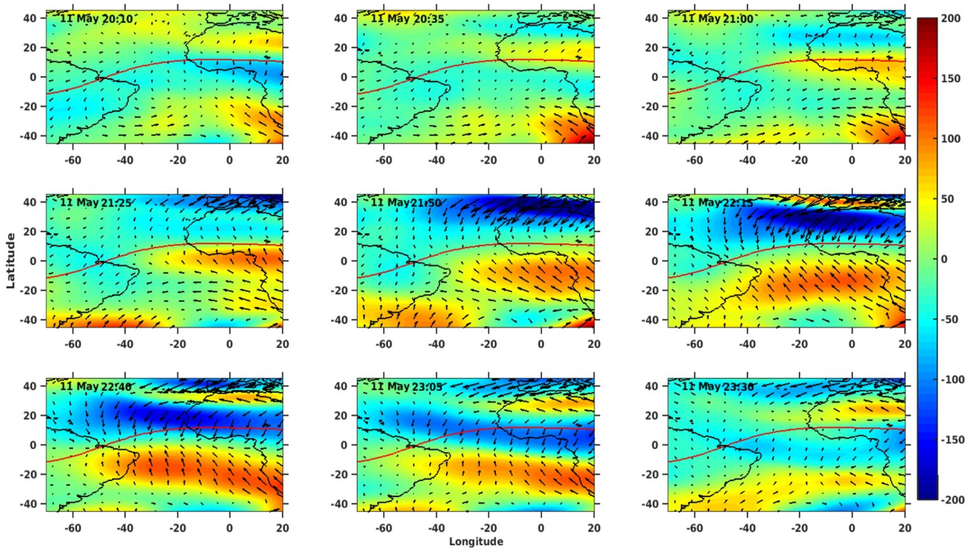

b) TIEGCM simulated electron density at ~320km

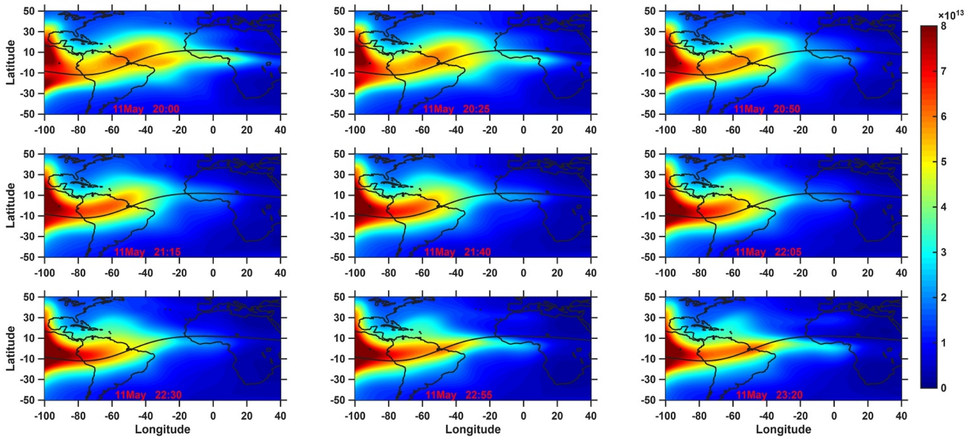

c) TIEGCM simulated thermospheric composition at ~180km

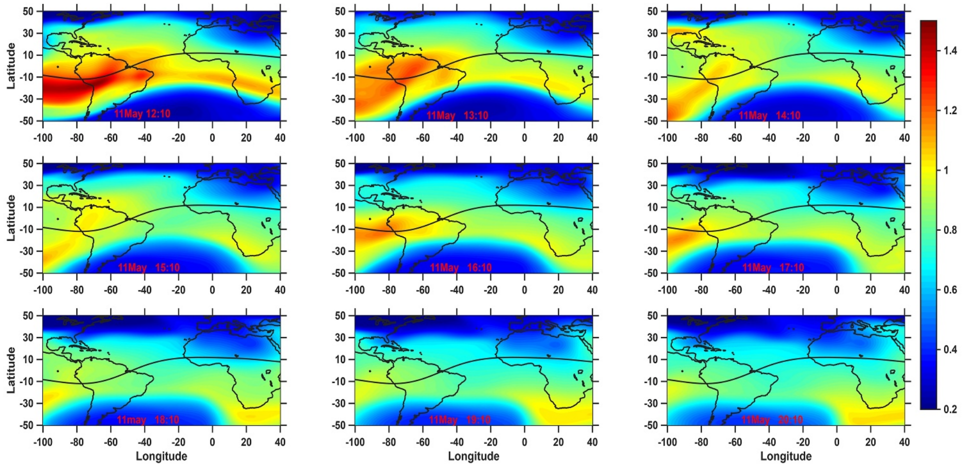

Figure 7. (a) Meridional wind obtained from TIEGCM simulation at ∼320 km altitude. Positive value indicates the wind is in northward and negative wind is in southward direction. (b) Total electron content obtained from TIEGCM simulation at ∼320 km altitude. (c) TIEGCM simulated $\Sigma O/N_2$ ratio at ∼180 km altitude. The time mentioned in the figure is in UT and the black line represents the geomagnetic equator.

climatological inputs. These combined factors likely contribute to the observed overestimation in the northern hemisphere.

3.6. The Inter Comparison of Observation and Simulation

To ensure the reliability of the observations, the simulation results are systematically compared with the GOLD measurements for both electron density and thermospheric composition. Figure S5 in Supporting Information S1 presents the colocation of electron density variations as derived from both the simulation and the observational data. In order to substantiate this agreement and provide a more rigorous comparison, we additionally extracted the latitude profiles at successive time intervals. These latitude profiles enabled a detailed intercomparison between the simulated and observed electron density, thereby ensuring a more comprehensive assessment of the consistency between the two data sets. Figure 8a presents the latitudinal profiles of the peak electron density derived from GOLD observations along with the TIEGCM-simulated electron density. The comparison is carried out for several fixed longitudes (with an interval of 3°) at different times. To enable a meaningful intercomparison, the electron density values are subjected to Z-score normalization (Vijayan & Shimna, 2021). The normalized profiles, along with the reported deviations between simulation and observation, highlight the degree of agreement. The deviation is smaller at the equatorial latitude, and it is higher in the midlatitude region. Importantly, the latitudinal locations of the electron density enhancements in both cases are well aligned, providing corroborative evidence that the simulation captures the observed large-scale features.

Similarly, the latitudinal profiles of thermospheric composition ($\Sigma O/N_2$) from GOLD observations are compared with the corresponding TIEGCM simulations for different times, using a fixed longitudinal interval of 5° (Figure 8b). The minor deviation between the observation and simulation at the equatorial latitudes indicates that the O/N_2 distributions also exhibit a consistent alignment in the latitude, further confirming that the simulation could reproduce the observed patterns of compositional variability.

4. Result and Discussion

The May 2024 superstorm, also known as the Gannon Superstorm (Evans et al., 2024), had a significant impact on the ionosphere-thermosphere system, altering plasma distribution across various ionospheric layers. The effects of the Gannon storm on the equatorial to low-mid latitude ionosphere have been examined from a number of different perspectives. For example, using GOLD observations Karan et al. (2024) reported the poleward shift of the EIA and its merging with the aurora due to the super-fountain effect during the main phase of the May 2024 storm. The shift in EIA crest toward farther latitudes typically occurs during an enhanced EEJ. This merging of the EIA southern crest with the aurora indicated the absence of the mid-latitude ionosphere during the main phase of the storm. Tulasi Ram et al. (2024) also reported intense enhancement in the TEC (more than 100%) in the dayside on 10 May.

In this study, we focus on the ionospheric response during the recovery phase. The GOLD data show an unusual pattern of plasma distribution, with very low peak electron density at low-mid latitudes and enhanced electron density along the geomagnetic equator (EIA trough) and complete absence of EIA crests (Figure 1).

A comparison of peak electron density variation between May 11 and 12 is presented in Supporting Information S1 (Figure S1). The comparison reveals that on May 11, electron density at the equatorial site is higher than at EIA crest positions. Similarly, the difference in $N_{\max}$ distribution between the storm day (11 May) and the next best quiet day after the storm (14 May) is presented in Figure S3 in Supporting Information S1. The result reveals positive values along the equator, thereby confirming the enhancement of $N_{\max}$ in the equatorial region on 11 May.

It is interesting to note that during the superstorm, the ionospheric plasma distribution in this sector showed a distinct behavior during each phase. During the main phase, the super-fountain effect caused a maximum poleward shift of the EIA crest, which merged with the auroral region (Karan et al., 2024), and the TEC increased by more than 100% (Tulasi Ram et al., 2024). On the following day, the initial recovery phase (11 May), the EIA crests disappeared completely along the equator (Figure 1). On the second recovery day (12 May), strong and well-separated EIA crests reappeared, with slight hemispheric asymmetry in intensity, the northern crest being weaker than the southern, a pattern also observed on the next best quiet day, 14 May. A similar pattern of TEC is observed in both GPS-based ground measurements (Figure 3) and the topside TEC from the Swarm satellite

a) Latitudinal profile of electron density

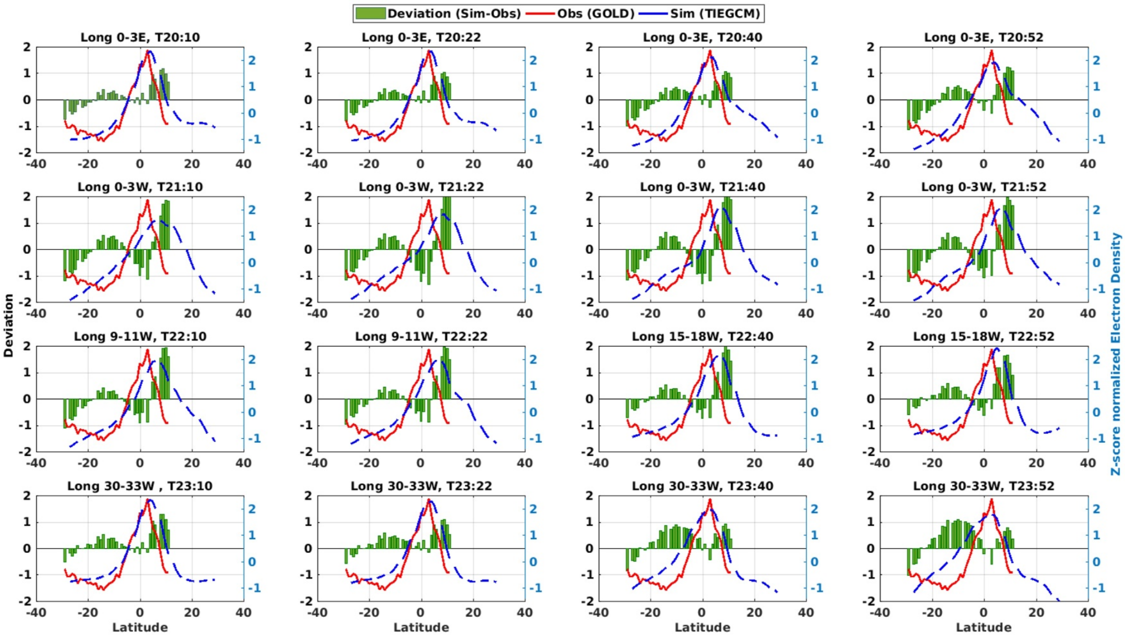

b) Latitudinal profile of thermospheric composition

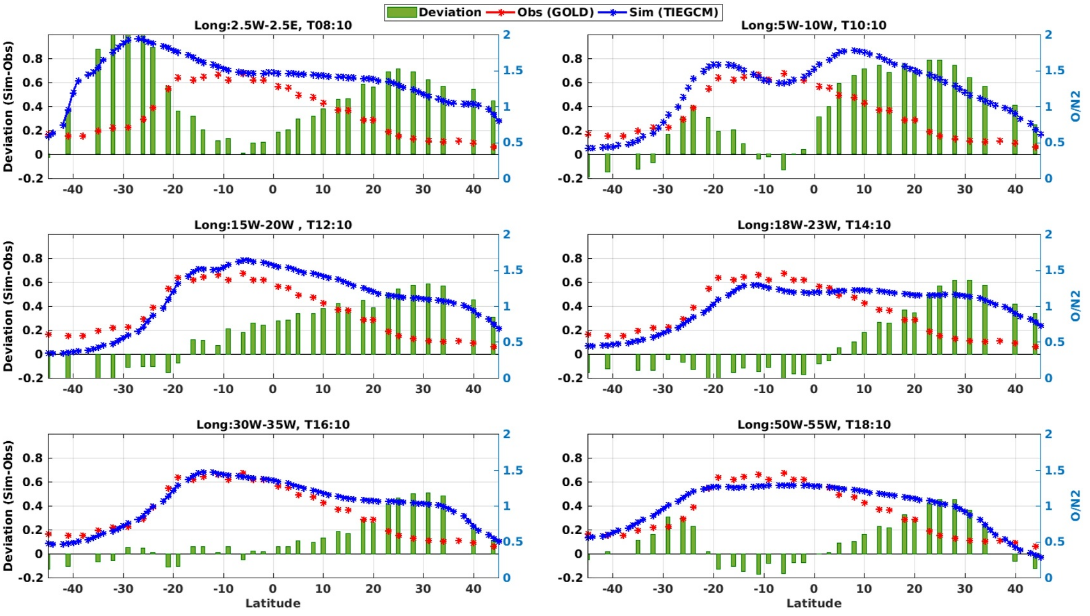

Figure 8. (a) Latitude profiles of TIEGCM-simulated electron density and GOLD $N_{\max}$ observations at different times. The longitude used for each profile is indicated in the respective plot. The deviation (simulation—observation) is shown on the left axis. The red and blue lines represent the z-score–normalized electron density of GOLD $N_{\max}$ and the TIEGCM simulation, respectively, on the right axis. (b) Latitude profiles of TIEGCM-simulated $\Sigma O/N_2$ and GOLD $\Sigma O/N_2$ observations at different times. The longitude used for each profile is indicated in the respective plot. The deviation (simulation—observation) is shown on the left axis. The red and blue lines represent the $\Sigma O/N_2$ of GOLD and the TIEGCM simulation, respectively, on the right axis.

(Figure 4). Although studies from the Chinese and Indian sectors reported negative ionospheric storm effects with low TEC values (Guo et al., 2024; A. Jain et al., 2024) associated with this storm, neither reported the absence of the EIA crest or the unusually enhanced TEC along the equator.

According to Li et al., 2019, Neutral winds constitute a key driver in the dynamics of the coupled thermosphere–ionosphere (TI) system. During geomagnetic storm conditions, the enhanced deposition of energy and momentum in the high-latitude upper thermosphere results in significant heating and increased ion drag. These processes alter the global circulation patterns of the neutral atmosphere, subsequently leading to variations in composition as well as neutral temperature. The joule heating in the polar region during geomagnetic storm induces temperature changes, and causes upward winds and upwelling of air such that the N_2-rich/O-poor air is bought up from the lower thermosphere (~100 km) into the *F* region (Burns, Killeen, Carignan, & Roble, 1995; Burns, Killeen, Deng, et al., 1995; Fuller-Rowell et al., 1994). At the same time, high-latitude temperature enhancement results in a strong equatorward horizontal pressure gradient and enhanced equatorward neutral winds to transmit the N_2-rich/O-poor air to the mid-low latitudes. This seems to imply that the large N_2 increases at high latitudes cause $\Sigma O/N_2$ depletion, which then extends to mid-low latitudes as the storms proceed (Kil et al., 2013; Meier, 2021). Whereas downwelling of air occurs at lower latitudes adjacent to the high latitude upwelling region due to thermospheric storm-time circulation changes. This storm-time downwelling of O-rich/N_2-poor air increases $\Sigma O/N_2$ (Burns, Killeen, Carignan, & Roble, 1995; Burns, Killeen, Deng, et al., 1995; Immel et al., 2001; Kil et al., 2013). $\Sigma O/N_2$ enhancement pattern is also propagated equatorward due to horizontal transport (Cai, Burns, Wang, Qian, Solomon, et al., 2021; Immel et al., 2008). The present analysis of the $\Sigma O/N_2$ ratio from the GOLD mission on May 11 is presented in Figure 5. An enhanced band of $\Sigma O/N_2$ appears to have moved toward and aligned along the equator over time, indicating strong equatorward winds as suggested by earlier studies. Similar patterns of equatorward enhancement are visible in the $N_{\max}$ measurements after 20:00 UT in GOLD, suggesting that the impact of the superstorm persisted for several hours, even during the recovery phase. Further, the storm time changes of peak electron density (Figure S7 in Supporting Information S1) obtained from TIEGCM simulation also show a clear enhancement along the equatorial region. A study by Evans et al. (2024), using GOLD $\Sigma O/N_2$ data, suggested that the observed intense variations in the $\Sigma O/N_2$ ratio is due to the temperature differences between the equator and high latitudes, caused by Joule heating, with a temperature difference of approximately 400 K. During intense geomagnetic storms, meridional winds extend to lower latitudes. At middle and low latitudes, vertical wind perturbations and the westward-directed Coriolis force dominate storm-time wind dynamics, influencing temperature and circulation patterns (Buonsanto, 1999; Gan et al., 2024; Meriwether, 2008). The storm time changes in the meridional wind obtained from TIEGCM simulation for 11 May is presented in Figure S6 in Supporting Information S1, which indicates presence of strong converging wind directed toward the equator from both hemispheres, due to a high-to-low latitude pressure gradient generated by high latitude heating (Babcock & Evans, 1979).

The absence of the EIA crests on May 11th could be attributed to the effects of an intense daytime counter-electrojet (CEJ) (~−100 nT) formed by strong DDEF, as observed in ground magnetic data (Figure 6). Although EEJ recovered around local noon time for a few hours around (15:00 UT) with a strength of ~60 nT, it seems to be insignificant or ineffective in causing fountain effects or meridional wind might have acted upon it.

The strong westward electric field associated with DDEF inhibited the necessary ExB drift for EIA formation. The unusually large CEJ observed during the morning to pre-noon hours is also evident in the ΔH data from TTB, provided in Figure 6. The depression in ΔH at TTB is more pronounced than at KOU (a low-latitude site). Additionally, the magnetic signature of ionospheric disturbances (DI) caused by electric field perturbations from high latitudes, shown in Figure 6, reveals a strong westward current at both KOU and TTB, which could indicate a DDEF. The intense CEJ is noted during 12:00 UT at TTB where no PPEF events are observed confirmed by Ey and modeled PEF (Figure 6a), while the magnetic signature associated with DI shows westward signatures at TTB confirm that the CEJ observed during the period caused by DDEF associated with Disturbance dynamo electric from the high latitude. A clear westward current at the low-latitude site KOU further confirms the presence of DDEF and exhibits an anti-Sq pattern. The low VTEC observed in the EIA crest region of the Indian sector on 11 May 2024, is also associated with DDEF as reported by Jain et al. (2024).

Earlier studies also have reported the absence of EIA crests and an enhancement of TEC along the equator, mostly during the recovery phase of geomagnetic storms. These studies discussed mechanisms involving CEJs caused by DDEF (Pincheira et al., 2002; Sreeja et al., 2009; Tulasi Ram et al., 2008). The present study also suggests the contribution of DDEF; however, unlike previous studies, we provide evidence of magnetic signatures associated with DDEF (Figure 6). Additionally, the present work examined the potential influence of thermospheric winds on the observed phenomena, supported by model simulations (Figure 7). Similar effects on electron density distribution were reported by Huang et al. (2010), who identified signatures of positive ionospheric storms along the magnetic equator near the post-sunset period, based on both theoretical and observational results. They concluded that such phenomena were seasonal and typically observed near the equinox, when summer-to-winter thermospheric winds were minimal. In contrast, the present study reported observations during the summer solstice, when hemispheric wind effects were expected to be strongest. The extreme intensity of the superstorm likely suppressed these seasonal wind patterns and resulted in converging winds along the equator. The drastic changes in $\Sigma O/N_2$ are also an indication of upwelling and downwelling processes caused by thermospheric wind due to Joule heating in the polar region.

The observed phenomena on 11 May, the first recovery day of Superstorm, is driven by thermospheric disturbance winds caused by joule heating, which is reflected as drastic change in $\Sigma O/N_2$, Disturbance dynamo induced CEJ. The meridional wind and TEC obtained from TIEGCM simulation provides the corroborative evidence for the observation. The strong equatorward converging winds observed from both high-latitude regions toward the equator might have gathered the distributed plasma, leading to an enhanced electron density along the geomagnetic equator, also in depletion of $\Sigma O/N_2$ ratio along high-mid-low latitudes and increase of $\Sigma O/N_2$ along equatorial latitudes. Additionally, the presence of a strong CEJ associated with Disturbance dynamo caused by thermospheric disturbance winds likely suppressed the formation of the equatorial fountain effect. Over time, the enhanced plasma along the equator dissipated completely, probably due to the downward ionospheric layer movement associated with the equatorial F-region dynamo.

5. Conclusion

The geomagnetic storm of 10–11 May 2024 exhibited diverse ionospheric responses across different regions of the globe, providing valuable insights into storm-time ionospheric dynamics during its various phases. Notably, during the recovery phase of the storm, an unusual enhancement in electron density was observed along with the absence of the typical EIA structure in the American sector. This anomalous behavior can be attributed to a complex interplay of factors, including storm-induced electrodynamic processes (such as CEJ and DDEF), changes in the thermospheric composition (e.g., altered $\Sigma O/N_2$ ratio), and the influence of strong equatorward meridional wind patterns generated by the storm. Together, these mechanisms contributed to the redistribution and modification of plasma in the equatorial and low-latitude ionosphere. The formation of a narrow region, an enhanced electron density band near the magnetic equator, is primarily due to the equatorward-converging meridional wind which arises from temperature gradients produced by Joule heating. Further, the equatorward wind inhibits the diffusion of plasma to low-latitude along the magnetic field lines. This enhancement dissipates within 1.5 hr, probably due to the downward ionospheric layer movement associated with the equatorial F-region dynamo, which brings the plasma to a region of higher recombination rates.

Furthermore, the consistency between observational data and simulation results strengthens these interpretations, as the simulations effectively captured key features of the severe May 2024 geomagnetic storm-induced ionospheric variability, including the enhanced electron density at the equator, the absence of EIA crests, and the presence of equatorward-converging meridional winds. Hence, this study provides valuable insights into the response of the equatorial and low-latitude ionosphere during the recovery phase of the severe solar disturbances, emphasizing the complex interactions between solar activity and Earth's upper atmosphere.

Conflict of Interest

The authors declare no conflicts of interest relevant to this study.

Data Availability Statement

The Level 2 N_{max} and ON_2 data used in this study are available at the GOLD Science Data Center (https://gold.cs.ucf.edu/data/search/). The GPS data is obtained from https://www.unavco.org/data/gps-gnss/data-access-methods/gnss-data-access-notebooks/gnss-permanent-station-data-access-notebook-embed.html. The INTERMAGNET data can be obtained from https://imag-data.bgs.ac.uk/GIN_V1/GINForms2. The TIEGCM data set used is available at Shimna and Lu (2025). The penetration electric field obtained from this Prompt Penetration Equatorial Electric Field Model (PPEEFM) over the longitude of 50°W was used in this study for comparison with ground-based magnetic observations. The model is accessible at https://geomag.colorado.edu/online-calculators/real-time-model-ionospheric-electric-fields. The Dst and Kp indices were also obtained from the OMNI website (https://omniweb.gsfc.nasa.gov/).

Acknowledgments

This research was supported by the Indian Space Research Organization. The authors K. Shimna and Archana R K duly acknowledge the financial support provided by Indian Space Research Organization as a fellowship. The authors would like to thank anonymous reviewers for their constructive comments on the manuscript.

References

Babcock, J. R. R., & Evans, J. V. (1979). Effects of geomagnetic disturbances on neutral winds and temperatures in the thermosphere observed over Millstone Hill. *Journal of Geophysical Research*, *84*(A9), 5349–5354. https://doi.org/10.1029/JA084iA09p05349

Bulusu, J., Archana, R. K., & Arora, K. (2020). Spatial variations in disturbance ionospheric currents—Inference from 12 geomagnetic storms. *Journal of Geophysical Research: Space Physics*, *125*(8), e2019JA027718. https://doi.org/10.1029/2019JA027718

Bulusu, J., RK, A., Arora, K., Chandrasekhar, N. P., & Nagarajan, N. (2018). Effect of disturbance electric fields on equatorial electrojet over Indian longitudes. *Journal of Geophysical Research: Space Physics*, *123*(7), 5894–5916. https://doi.org/10.1029/2018JA025247

Buonsanto, M. J. (1999). Ionospheric storms—A review. *Space Science Reviews*, *88*(3/4), 563–601. https://doi.org/10.1023/A:1005107532631

Burns, A. G., Killeen, T. L., Carignan, G. R., & Roble, R. G. (1995). Large enhancements in the O/N_2 ratio in the evening sector of the winter hemisphere during geomagnetic storms. *Journal of Geophysical Research*, *100*(A8), 14661–14671. https://doi.org/10.1029/94ja03235

Burns, A. G., Killeen, T. L., Deng, W., Carignan, G. R., & Roble, R. G. (1995). Geomagnetic storm effects in the low-to middle-latitude upper thermosphere. *Journal of Geophysical Research*, *100*(A8), 14673–14691. https://doi.org/10.1029/94ja03232

Cai, X., Burns, A. G., Wang, W., Qian, L., Liu, J., Solomon, S. C., et al. (2021). Observation of postsunset OI 135.6 nm radiance enhancement over South America by the GOLD mission. *Journal of Geophysical Research: Space Physics*, *126*(2), e2020JA028108. https://doi.org/10.1029/2020ja028108

Cai, X., Burns, A. G., Wang, W., Qian, L., Pedatella, N., Coster, A., et al. (2021). Variations in thermosphere composition and ionosphere total electron content under "geomagnetically quiet" conditions at solar-minimum. *Geophysical Research Letters*, *48*(11), e2021GL093300. https://doi.org/10.1029/2021GL093300

Cai, X., Burns, A. G., Wang, W., Qian, L., Solomon, S. C., Eastes, R. W., et al. (2020). The two-dimensional evolution of thermospheric O/N_2 response to weak geomagnetic activity during solar-minimum observed by GOLD. *Geophysical Research Letters*, *47*(18), e88838. https://doi.org/10.1029/2020GL088838

Cai, X., Burns, A. G., Wang, W., Qian, L., Solomon, S. C., Eastes, R. W., et al. (2021). Investigation of a neutral "Tongue" observed by GOLD during the geomagnetic storm on May 11, 2019. *Journal of Geophysical Research: Space Physics*, *126*(6), e2020JA028817. https://doi.org/10.1029/2020JA028817

Catherine, J. K., Vijayan, M. S. M., Rabiya, U. S., Shimna, K., Gahalaut, V. K., & Ramesh, D. S. (2015). Dichotomy in mode propagation of coseismic ionospheric disturbance: Observations from 11 April 2012 Indian Ocean earthquake. *Journal of Geophysical Research: Space Physics*, *120*(5), 3854–3867. https://doi.org/10.1002/2014JA020621

Clauer, C. R., McPherron, R. L., & Kivelson, M. G. (1980). Uncertainty in ring current parameters due to the quiet magnetic field variability at mid-latitudes. *Journal of Geophysical Research*, *85*(A2), 633–643. https://doi.org/10.1029/JA085iA02p00633

Correira, J., Evans, J. S., Lumpe, J., Krywonos, A., Daniell, R., Veibell, V., et al. (2021). Thermospheric composition and solar EUV flux from the global-scale observations of the limb and disk (GOLD) mission. *Journal of Geophysical Research: Space Physics*, *126*(12), e2021JA029517. https://doi.org/10.1029/2021ja029517

DeMajistre, R., Paxton, L. J., Morrison, D., Yee, J.-H., Goncharenko, L. P., & Christensen, A. B. (2004). Retrievals of nighttime electron density from thermosphere ionosphere mesosphere energetics and dynamics (TIMED) mission global ultraviolet imager (GUVI) measurements. *Journal of Geophysical Research*, *109*(A5), A05305. https://doi.org/10.1029/2003JA010296

Eastes, R. W., McClintock, W. E., Burns, A. G., Anderson, D. N., Andersson, L., Codrescu, M., et al. (2017). The global-scale observations of the limb and disk (GOLD) mission. *Space Science Reviews*, *212*(1–2), 383–408. https://doi.org/10.1007/s11214-017-0392-2

Eastes, R. W., Solomon, S. C., Daniell, R. E., Anderson, D. N., Burns, A. G., England, S. L., et al. (2019). Global-scale observations of the equatorial ionization anomaly. *Geophysical Research Letters*, *46*(16), 9318–9326. https://doi.org/10.1029/2019gl084199

Evans, J. S., Strickland, D., & Huffman, R. (1995). Satellite remote sensing of thermospheric O/N_2 and solar EUV. 2: Data analysis. *Journal of Geophysical Research*, *100*(A7), 12227–12233. https://doi.org/10.1029/95JA00573

Evans, J. S., Correira, J., Lumpe, J. D., Eastes, R. W., Gan, Q., Laskar, F. I., et al. (2024). GOLD observations of the thermospheric response to the 10–12 May 2024 Gannon superstorm. *Geophysical Research Letters*, *51*(16), e2024GL110506. https://doi.org/10.1029/2024GL110506

Fuller-Rowell, T. J., Codrescu, M. V., Moffett, R. J., & Quegan, S. (1994). Response of the thermosphere and ionosphere to geomagnetic storms. *Journal of Geophysical Research*, *99*(A3), 3893–3914. https://doi.org/10.1029/93ja02015

Gan, Q., Eastes, R. W., Wu, Y.-J., Qian, L., Cai, X., Wang, W., et al. (2024). Thermospheric responses to the 3 and 4 November 2021 geomagnetic storm during the main and recovery phases as observed by NASA's GOLD and ICON missions. *Geophysical Research Letters*, *51*(4), e2023GL106529. https://doi.org/10.1029/2023GL106529

Guo, X., Zhao, B., Yu, T., Hao, H., Sun, W., Wang, G., et al. (2024). East–west difference in the ionospheric response during these recovery phase of May 2024 super geomagnetic storm over the East Asian. *Journal of Geophysical Research: Space Physics*, *129*(9), e2024JA033170. https://doi.org/10.1029/2024JA033170

Huang, C. M., Chen, M. Q., & Liu, J. Y. (2010). Ionospheric positive storm phases at the magnetic equator close to sunset. *Journal of Geophysical Research*, *115*(A7), A07315. https://doi.org/10.1029/2009JA014936

Immel, T. J., Crowley, G., Craven, J. D., & Roble, R. G. (2001). Dayside enhancements of thermospheric O/N_2 following magnetic storm onset. *Journal of Geophysical Research*, *106*(A8), 15471–15488. https://doi.org/10.1029/2000JA000096

Immel, T. J., Forbes, J. M., Nerem, R. S., Sutton, E. K., & Crowley, G. (2008). Neutral composition and density effects in the October–November 2003 magnetic storms this storm, this volume.

Jain, A., Trivedi, R., Jain, S., & Choudhary, R. (2024). Effects of the super intense geomagnetic storm on 10–11 May, 2024 on total electron content at Bhopal. *Advances in Space Research*, *75*(1), 953–965. https://doi.org/10.1016/j.asr.2024.09.029

Karan, D. K., Martinis, C. R., Daniell, R. E., Eastes, R. W., Wang, W., McClintock, W. E., et al. (2024). GOLD observations of the merging of the Southern Crest of the equatorial ionization anomaly and aurora during the 10 and 11 May 2024 Mother's Day super geomagnetic storm. *Geophysical Research Letters*, *51*(15), e2024GL110632. https://doi.org/10.1029/2024gl110632

Katus, R. M., & Liemohn, M. W. (2013). Similarities and differences in low- to middle-latitude geomagnetic indices. *Journal of Geophysical Research: Space Physics*, *118*(8), 5149–5156. https://doi.org/10.1002/jgra.50501

Kil, H., Lee, W. K., Shim, J., Paxton, L. J., & Zhang, Y. (2013). The effect of the 135.6 nm emission originated from the ionosphere on the TIMED/GUVI O/N_2 ratio. *Journal of Geophysical Research: Space Physics*, *118*(2), 859–865. https://doi.org/10.1029/2012JA018112

Le Huy, M., & Amory-Mazaudier, C. (2005). Magnetic signature of the ionospheric disturbance dynamo at equatorial latitudes: "Ddyn". *Journal of Geophysical Research*, *110*(A10). https://doi.org/10.1029/2004ja010578

Li, J., Wang, W., Lu, J., Yue, J., Burns, A. G., Yuan, T., et al. (2019). A modeling study of the responses of mesosphere and lower thermosphere winds to geomagnetic storms at middle latitudes. *Journal of Geophysical Research: Space Physics*, *124*(5), 3666–3680. https://doi.org/10.1029/2019JA026533

Manoj, C., & Maus, S. (2012). A real-time forecast service for the ionospheric equatorial zonal electric field. *Space Weather*, *10*(9). https://doi.org/10.1029/2012SW000825

Manoj, C., Maus, S., Lühr, H., & Alken, P. (2008). Penetration characteristics of the interplanetary electric field to the daytime equatorial ionosphere. *Journal of Geophysical Research*, *113*(A12). https://doi.org/10.1029/2008JA013381

McClintock, W. E., Eastes, R. W., Beland, S., Bryant, K. B., Burns, A. G., Correira, J., et al. (2020). Global-scale observations of the limb and disk mission implementation: 2. Observations, data pipeline, and level 1 data products. *Journal of Geophysical Research: Space Physics*, *125*(5), e2020JA027809. https://doi.org/10.1029/2020ja027809

Meier, R. R. (2021). The thermospheric column O/N_2 ratio. *Journal of Geophysical Research: Space Physics*, *126*(3), e2020JA029059. https://doi.org/10.1029/2020JA029059

Meriwether, J. W. (2008). Thermospheric dynamics at low and mid-latitudes during magnetic storm activity. In *Geophysical monograph series* (Vol. 181, pp. 201–219). https://doi.org/10.1029/181GM19

Peltier, A., & Chulliat, A. (2010). On the feasibility of promptly producing quasi-definitive magnetic observatory data. *Earth Planets and Space*, *62*(2), e5–e8. https://doi.org/10.5047/eps.2010.02.002

Pincheira, X. T., Abdu, M. A., Batista, I. S., & Richards, P. G. (2002). An investigation of ionospheric responses, and disturbance thermospheric winds, during magnetic storms over South America sector. *Journal of Geophysical Research*, *107*(A11), 1379. https://doi.org/10.1029/2001JA000263

Qian, L., Burns, A. G., Emery, B. A., Foster, B., Lu, G., Maute, A., et al. (2014). The NCAR TIE-GCM: A community model of the coupled thermosphere/ionosphere system. In *Modeling the ionosphere–thermosphere system* (pp. 73–83).

Richmond, A. D., & Kamide, Y. (1988). Mapping electrodynamic features of the high-latitude ionosphere from localized observations: Technique. *Journal of Geophysical Research*, *93*(A6), 5741–5759. https://doi.org/10.1029/ja093ia06p05741

Richmond, A. D., Ridley, E. C., & Roble, R. G. (1992). A thermosphere/ionosphere general circulation model with coupled electrodynamics. *Geophysical Research Letters*, *19*(6), 601–604. https://doi.org/10.1029/92GL00401

Roble, R. G., Ridley, E. C., Richmond, A. D., & Dickinson, R. E. (1988). A coupled thermosphere/ionosphere general circulation model. *Geophysical Research Letters*, *15*(12), 1325–1328. https://doi.org/10.1029/GL015i012p01325

Rout, D., Kumar, A., Singh, R., Patra, S., Karan, D. K., Chakraborty, S., et al. (2024). Evidence of unusually strong equatorial ionization anomaly at three local time sectors during the mother's day geomagnetic storm on 10–11 May 2024. *Geophysical Research Letters*, *52*(2), e2024GL111269. https://doi.org/10.1029/2024gl111269

Shimna, K., & Lu, G. (2025). Impact of the Gannon superstorm on the equatorial ionization anomaly dynamics during the recovery phase on May 11, 2024 [Dataset]. In *Impact of the Gannon superstorm on the equatorial ionization anomaly dynamics during the recovery phase on May 11, 2024*. Zenodo. https://doi.org/10.5281/zenodo.15645950

Shimna, K., & Vijayan, M. S. M. (2020). Detecting ionospheric disturbances using GPS without aliasing caused by non-uniform spatial sampling: Algorithm, validation and illustration. *Journal of Atmospheric and Solar-Terrestrial Physics*, *209*, 105400. https://doi.org/10.1016/j.jastp.2020.105400

Sreeja, V., Ravindran, S., Pant, T. K., Devasia, C. V., & Paxton, L. J. (2009). Equatorial and low-latitude ionosphere-thermosphere system response to the space weather event of August 2005. *Journal of Geophysical Research*, *114*(A12), A12307. https://doi.org/10.1029/2009JA014491

Strickland, D. J., Evans, J. S., & Paxton, L. J. (1995). Satellite remote sensing of thermospheric O/N_2 and solar EUV. 1: Theory. *Journal of Geophysical Research*, *100*(A7), 12217–12226. https://doi.org/10.1029/95JA00574

Themens, D. R., Elvidge, S., McCaffrey, A., Jayachandran, P. T., Coster, A., Varney, R. H., et al. (2024). The high latitude ionospheric response to the major May 2024 geomagnetic storm: A synoptic view. *Geophysical Research Letters*, *51*(19), e2024GL111677. https://doi.org/10.1029/2024GL111677

Tulasi Ram, S., Rama Rao, P. V. S., Prasad, D. S. V. V. D., Niranjan, K., Gopi Krishna, S., Sridharan, R., & Ravindran, S. (2008). Local time dependent response of postsunset ESF during geomagnetic storms. *Journal of Geophysical Research*, *113*(A7), A07310. https://doi.org/10.1029/2007JA012922

Tulasi Ram, S., Veenadhari, B., Dimri, A. P., Bulusu, J., Bagiya, M., Gurubaran, S., et al. (2024). Super-intense geomagnetic storm on 10–11 May 2024: Possible mechanisms and impacts. *Space Weather*, *22*(12), e2024SW004126. https://doi.org/10.1029/2024sw004126

Vijayan, M. S. M., & Shimna, K. (2022). Detecting aliasing and artifact free co-seismic and tsunamigenic ionospheric perturbations using GPS. *Advances in Space Research*, *69*(2), 951–975. https://doi.org/10.1016/j.asr.2021.10.040

Vijayan, M. S. M., Varghese, G., & Shimna, K. (2013). IONODETECT: A software to compute ionospheric TEC perturbations using dual frequency geodetic GPS data. In *Annual Report 2012–2013*. CSIR 4PI. Retrieved from http://csir4pi.in/images/20132013_annual.pdf

Yadav, S., Choudhary, R. K., Kumari, J., Sunda, S., Shreedevi, P. R., & Pant, T. K. (2020). Reverse fountain and the nighttime enhancement in the ionospheric electron density over the equatorial region: A case study. *Journal of Geophysical Research: Space Physics*, *125*(5), e2019JA027286. https://doi.org/10.1029/2019JA027286

Zhang, R., Liu, L., Le, H., Chen, Y., & Kuai, J. (2017). The storm time evolution of the ionospheric disturbance plasma drifts. *Journal of Geophysical Research: Space Physics*, *122*(11), 11665–11676. https://doi.org/10.1002/2017JA024637

Zhang, R., Liu, L., Yang, Y., Li, W., Zhao, X., Yoshikawa, A., et al. (2024). Ionosphere responses over Asian-Australian and American sectors to the 10–12 May 2024 superstorm. *Journal of Geophysical Research: Space Physics*, *129*(12), e2024JA033071. https://doi.org/10.1029/2024ja033071

Zhang, R., Liu, L., Yue, X., Zhang, J., Zhang, N., Chen, Y., et al. (2025). The penetration electric fields during the 10 May 2024 superstorm observed by ISRs over Sanya and Jicamarca. *Geophysical Research Letters*, *52*(6), e2024GL114543. https://doi.org/10.1029/2024GL114543